

# A Novel Adaptive Filtering-Based Tuning Loop for High-Q SRF Cavity

Yubing Shen,<sup>1,2</sup> Qiang Gu,<sup>3</sup> Xiang Zheng,<sup>3</sup> and Xuefang Huang<sup>3</sup>

<sup>1</sup>Shanghai Institute of Applied Physics, Chinese Academy of Sciences, Shanghai 201800, China

<sup>2</sup>University of Chinese Academy of Sciences, Beijing 100049, China

<sup>3</sup>Shanghai Advanced Research Institute, Chinese Academy of Sciences, Shanghai 201210, China

The Shanghai HIgh repetitioN rate XFEL and Extreme light facility (SHINE) utilizes high-Q  $1.3\text{GHz}$  superconducting radio-frequency (SRF) cavities for particle acceleration. These cavities, with an ultra-narrow bandwidth of approximately  $32\text{Hz}$ , are highly susceptible to Lorentz force detuning (LFD) and microphonics, which can destabilize the cavity resonance frequency and compromise system performance. This paper presents a novel detuning compensation scheme that combines an autoregressive least-mean-square (LMS) adaptive filter and active noise control (ANC) in a parallel configuration to mitigate microphonic-induced detuning. A real-time simulation model, incorporating the cavity's mechanical eigenmodes, was developed to evaluate the proposed approach. Simulation results demonstrate significant reductions in amplitude and phase errors by approximately 90% and 70%, respectively, compared to the open-loop tuning configuration, achieving the stringent operational requirements. This study introduces an innovative detuning compensation strategy for high-Q SRF cavities, providing a robust framework for optimizing RF system design and ensuring stability in complex noise environments.

Keywords: Microphonics, RF cavity model, Tuning Loop

## I. INTRODUCTION

Superconducting radio-frequency (SRF) cavities are widely employed in modern particle accelerators [1][2][3]. Their high Q-factor design significantly reduces the operational costs of high-power systems but also introduces the risk of detuning due to their extremely narrow bandwidth [4][5]. Under high-load operating conditions, even minor frequency deviations can substantially impact the amplitude and phase stability within the cavity, leading to a significant increase in power demands [6][7][8]. In such scenarios, greater attention must be directed toward the tuning loop, requiring faster response times to compensate for detuning frequencies caused by external disturbances.

Cavity detuning primarily arises from two factors: Lorentz Force Detuning (LFD) and microphonics. LFD, caused by the interaction between the electromagnetic field and wall currents, deforms the cavity and excites mechanical modes. However, when operating in continuous-wave (CW) mode, LFD can be effectively mitigated by pre-setting cavity detuning compensation in advance [9][10]. Microphonics, on the other hand, which has a significant impact in CW mode [11], includes deterministic disturbances such as those from cryogenic systems and vacuum pumps. These can be compensated using Active Noise Control (ANC), a method validated in facilities like Linac Coherent Light Source II (LCLS-II) [12]. For stochastic factors such as ground vibrations, adaptive filters are currently the most viable compensation approach. These detuning challenges demand fast response capabilities from the tuning loop. Taking Shanghai High repetition rate XFEL and Extreme light facility (SHINE) as an example, the target is to maintain the Root Mean Square (RMS) detuning frequency below  $1.5\text{Hz}$  [13]. Of course, there are also other methods, such

as Disturbance Observer-Based control (DOB) and Iterative Learning Control (ILC) [14] [15], feedforward-based control [16], and Active Disturbance Rejection Control (ADRC) [17][18], among others.

To verify the effectiveness of various control measurements and algorithms in meeting the voltage stability requirements within the RF cavity, it is necessary to establish a real-time cavity simulation [19]. In addition to incorporating the cavity equivalent model and amplitude-phase feedback loops, it is crucial to develop a comprehensive and accurate tuning loop model. The tuning actuators responsible for compensating cavity detuning frequencies include stepper motor for slow tuning and piezo for fast tuning [20][21]. Both the piezo and the mechanical eigenmodes of the cavity are considered in the model. Using SHINE accelerating cavities as an example, control parameters are ultimately adjusted to achieve an RMS voltage amplitude stability of less than 0.02% and an RMS phase stability of less than  $0.02^\circ$ .

The structure of this paper is as follows: It begins with a detailed discussion of the sources of detuning in high-Q SRF cavities, focusing on the characteristics of microphonics and its impact on cavity stability. Sec. II evaluates various tuning loop control strategies and selects the Least Mean Squares (LMS) algorithm as the core for detuning compensation, analyzing potential instabilities in combination with system characteristics. Sec. III establishes a real-time simulation model incorporating the mechanical eigenmodes of the cavity to verify the effectiveness of different control strategies, with an in-depth analysis of the combined effects of ANC and LMS on suppressing amplitude and phase errors. Sec. IV concludes the paper.

69

## II. CONTROL STRATEGY

### 70 A. Cavity Detuning Frequency and Changes in Control 71 Strategies

72 In traditional normal conducting RF cavities or low-Q  
73 superconducting RF cavities, the tuning loop response  
74 frequency is typically designed to be relatively low to  
75 avoid coupling with the amplitude-phase loop [22]. For  
76 instance, the SSRF 500MHz superconducting cavity has  
77 a half-bandwidth of approximately 1.25kHz. In such  
78 cases, detuning of a few Hz has minimal impact on the  
79 amplitude-phase stability of the accelerating field inside  
80 the cavity. Therefore, a slow tuning loop with a re-  
81 sponse frequency of about 1–10Hz is sufficient, while the  
82 amplitude-phase loop bandwidth generally ranges from  
83 0.1 – 4kHz [23].

84 In contrast, the SHINE main accelerating cavity has  
85 a resonance frequency of 1300 MHz and a loaded Q-  
86 factor as high as  $4 \times 10^7$ , resulting in a half-bandwidth  
87 of only about 16.25Hz [24]. Under these conditions, de-  
88 tuning of just a few Hz can significantly degrade the  
89 amplitude-phase stability of the accelerating field, ne-  
90 cessitating real-time compensation via fast tuning loop.  
91 However, simply increasing the tuning loop bandwidth  
92 may result in coupling with the amplitude-phase loop,  
93 and when the bandwidth reaches the scale of hundreds  
94 of Hz, it can even lead to system instability [25][26].

95 We enabled the amplitude-phase loop with small gain  
96 in SHINE RF cavity test, when the RF cavity was op-  
97 erating roughly in the steady-state region, utilizing the  
98 widely adopted Schilcher cavity model based on state-  
99 space representation to inversely calculate the cavity de-  
100 tuning frequency [27][28][29]:

$$\begin{pmatrix} V'_{C,r}(t) \\ V'_{C,i}(t) \end{pmatrix} = \begin{pmatrix} -\omega_{1/2} & -\Delta\omega \\ \Delta\omega & -\omega_{1/2} \end{pmatrix} \begin{pmatrix} V_{C,r}(t) \\ V_{C,i}(t) \end{pmatrix} + \frac{2\beta}{\beta+1} \begin{pmatrix} \omega_{1/2} & 0 \\ 0 & \omega_{1/2} \end{pmatrix} \begin{pmatrix} V_{f,r}(t) \\ V_{f,i}(t) \end{pmatrix}, \quad (1)$$

101  $V_C$  and  $V_f$  represent the cavity voltage and input voltage,  
102 respectively. The subscripts  $r$  and  $i$  indicate the real and  
103 imaginary components.  $\omega_{1/2}$  represents the cavity half-  
104 bandwidth,  $\Delta\omega$  is the cavity detuning angular frequency,  
105 and  $\beta$  is the coupling coefficient, which is typically much  
106 greater than 1 in high-Q loaded cavities. Under CW  
107 operation mode, the cavity detuning angular frequency  
108 at a steady state at time  $n$  can be expressed as:

$$\Delta\omega(n) = \frac{2\beta}{\beta+1} \frac{\omega_{1/2}}{V_{C,r}^2(n) + V_{C,i}^2(n)} \times (V_{C,i}(n) V_{f,r}(n) - V_{C,r}(n) V_{f,i}(n)). \quad (2)$$

111 Under steady-state operating conditions, the time-  
112 domain and frequency-domain plots of cavity detuning  
113 frequency are shown in Fig. 1. Since the impact of LFD  
114 under steady-state CW operation is negligible [30], the  
115 detuning is primarily caused by microphonics. During

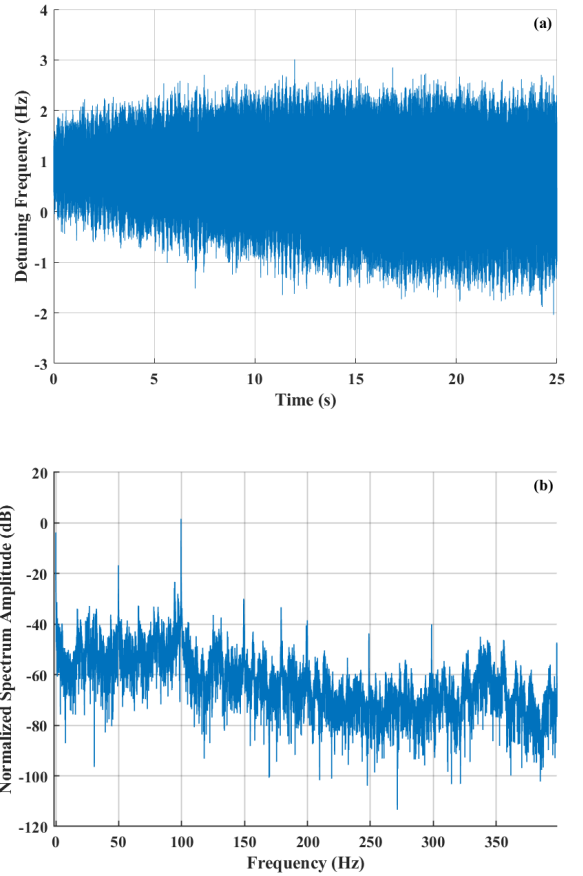


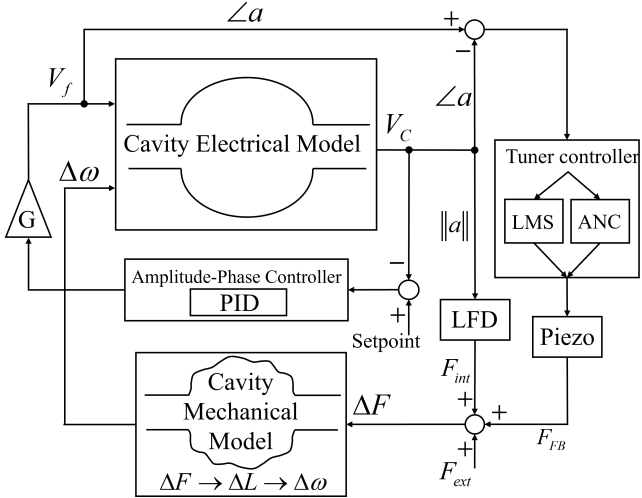
Fig. 1. (Color online) Time-domain (a) and frequency-  
domain (b) representations of the cavity detuning frequency.

116 the prolonged testing, it was observed that the frequency  
117 detuning remained relatively stable within the range of  
118 –3Hz to +3Hz. A 25-second sample was selected for  
119 analysis. Fig. 1(a) shows the time-domain spectrum of  
120 the frequency detuning. During this period, the detun-  
121 ing frequency may exhibit a slight increase, potentially  
122 due to the influence of external ground vibrations. This  
123 sudden change further highlights the generalization abil-  
124 ity and adaptability of the tuning algorithm in respond-  
125 ing to external disturbances. Fig. 1(b) presents the  
126 frequency-domain spectrum of the frequency detuning,  
127 By analyzing the spectral plot of the detuning frequency,  
128 its primary characteristics can be identified. Prominent  
129 spectral components are observed at DC and specific fre-  
130 quency points. After shutting off the vacuum pump, the  
131 50Hz and nearby vibrational noise interference signifi-  
132 cantly decreased, indicating that the noise in certain fre-  
133 quency bands is caused by mechanical vibrations from  
134 components. When these devices are turned off, the cor-  
135 responding noise levels are notably reduced. This sug-  
136 gests that optimizing noise sources to minimize mechan-  
137 ical vibrations is an effective mitigation strategy. Addi-  
138 tionally, control algorithms targeting specific frequency  
139 points, such as ANC, can be employed to further sup-

141 press these noise components.

142 Second, the remaining spectral components are mainly  
143 distributed below 250Hz, where scattered random noise  
144 dominates. This frequency range also coincides with the  
145 mechanical eigenmodes of the cavity. The next section  
146 will focus on the use of real-time adaptive filters to sup-  
147 press noise within this frequency band.

148 In summary, the proposed control logic block diagram  
149 is presented in Fig. 2.



150 Fig. 2. Control logic block diagram of the system loop.

151 Here,  $|a|$  denotes the magnitude, and  $\angle a$  represents  
152 the phase angle. The amplitude-phase loop employs PID  
153 control, while the tuning loop adopts a real-time adap-  
154 tive filter combined with the ANC for better suppression  
155 of cavity detuning. Regardless of the source of noise, the  
156 process ultimately applies forces to the cavity, causing  
157 deformation and resulting in changes to the cavity's res-  
158 onant frequency. This process is modeled in the Cav-  
159 ity Mechanical Model block, which will be discussed in  
160 greater detail in Sec. III. The Lorentz force generated  
161 by RF fields is referred to as  $F_{int}$ , while the force caused  
162 by microphonics is denoted as  $F_{ext}$ . The feedback loop  
163 applies a force through the piezo, which is labeled as  
164  $F_{FB}$ .

## 166 B. Control Algorithm

167 An adaptive filter is a dynamic filter capable of auto-  
168 matically adjusting its parameters based on changes in  
169 the input signal. Its core functionality lies in minimizing  
170 the error signal through iterative algorithms, enabling  
171 effective signal extraction and noise suppression. Un-  
172 like traditional fixed-parameter filters, adaptive filters  
173 do not require pre-defined filtering parameters. Instead,  
174 they utilize algorithmic optimization techniques to dy-  
175 namically update filter coefficients in real-time, allowing  
176 them to adapt to time-varying signal environments [31].

177 If cavity frequency detuning is considered as interfer-  
178 ence noise, suppressing this noise typically requires a ref-  
179 erence noise signal that is correlated with the target noise  
180 to be suppressed. In the RF cavity operating environ-  
181 ment, the reference noise signal can be selected as the  
182 previously suppressed noise from the last time step, im-  
183 plementing an uncommon autoregressive strategy.

184 To evaluate the effectiveness of this control strategy,  
185 this study uses a single-tone 20Hz signal with a signal-  
186 to-noise ratio (SNR) of 30 as the test signal. The signal  
187 is subjected to autoregressive suppression using three dif-  
188 ferent adaptive filtering methods: LMS adaptive filter,  
189 Recursive Least Squares (RLS) filter, and Kalman adap-  
190 tive filter.

$$191 \begin{cases} w_n = [w_0(n), w_1(n), \dots, w_{N-1}(n)]^T \\ x_n = [x(n), x(n-1), \dots, x(n-N+1)]^T \\ y(n) = \sum_{i=0}^{N-1} x(n-i) \cdot w(i) = x_n^T \cdot w_n \\ x(n+1) = e(n) = d(n) - y(n) \end{cases}, \quad (3)$$

192 In this FIR filter, the filter coefficients  $w_n$  are updated  
193 at each time step, representing the filter weights at the  
194 current time, the length of this weight vector is  $N$ , which  
195 includes the filter coefficients from the current time step  
196 and the previous  $N-1$  time steps. The reference noise  
197 signal  $x_n$  is an input vector containing the current time  
198 step and the previous  $N-1$  time steps, with a length of  
199  $N$ . It represents the historical data used for noise sup-  
200 pression. The output of the filter,  $y(n)$ , is calculated by  
201 taking the dot product of the current filter coefficients  
202  $w_n$  and the reference noise signal  $x_n$ . Meanwhile, the  
203 difference between the filter output and the desired out-  
204 put  $d(n)$  forms the error  $e(n)$ , which is also the reference  
205 signal  $x(n+1)$  for the next time step. This error is  
206 used to adjust and update the filter coefficients  $w_n$ . By  
207 continuously updating these filter coefficients, the FIR  
208 filter is able to progressively suppress noise and optimize  
209 based on new input data, thus achieving effective noise  
210 suppression.

$$211 w_{n+1} = w_n + \mu e(n) x_n. \quad (4)$$

212 Eq. 4 represents the basic form of the LMS filter,  
213 where the only parameter requiring initial configuration  
214 is the learning rate  $\mu$ .

$$215 \begin{cases} K_n = \frac{P_n x_n}{\lambda + x_n^T P_n x_n} \\ w_{n+1} = w_n + K_n e(n) \\ P_{n+1} = \frac{1}{\lambda} (P_n - K_n x_n^T P_n) \end{cases}. \quad (5)$$

216 Eq. 5 represents the basic form of the RLS filter,  $K_n$  is  
217 the RLS gain, which determines the step size for weight  
218 updates, thereby affecting the rate of adjustment of the  
219 filter coefficients. The covariance matrix  $P_n$  describes  
220 the uncertainty of the model parameters at the  $n$ -th time  
221 step. When  $P_n$  is large, it indicates higher uncertainty  
222 in the parameter estimates, resulting in a larger  $K_n$  and  
223 a larger weight update step. This is typically applicable  
224 in the early stages of model development or when the

225 data exhibits high variability. When  $P_n$  is small, the  
 226 current parameter estimates are more certain, leading to  
 227 a smaller  $K_n$  and a smaller weight update step. The for-  
 228 getting factor  $\lambda$  controls the influence of historical data  
 229 on model updates. If  $\lambda$  is large (close to 1), the algo-  
 230 rithm places more weight on historical data, making it  
 231 suitable for systems with slow changes. If  $\lambda$  is small, the  
 232 algorithm focuses more on the current data, making it  
 233 suitable for systems with rapid changes.

$$234 \quad \begin{cases} P_{n|n-1} = P_{n-1|n-1} + Q \\ K_n = P_{n|n-1} x_n (x_n^T P_{n|n-1} x_n + R)^{-1} \\ w_{n+1} = w_n + K_n e(n) \\ P_{n|n} = (I - K_n x_n^T) P_{n|n-1} \end{cases} . \quad (6)$$

235 Eq. 6 represents the basic form of the Kalman filter.  
 236 The Kalman gain  $K_n$  is similar to the RLS gain, deter-  
 237 mining the step size for weight updates. The left and  
 238 right sides of the subscript | represent state estimates at  
 239 different time points. Specifically, the left side refers to  
 240 the current state estimate, while the right side indicates  
 241 the estimate updated or predicted based on past infor-  
 242 mation or observations. For instance,  $P_{n|n-1}$  represents  
 243 the covariance matrix at time  $n$  based on the state es-  
 244 timate and prediction model from time  $n - 1$ , reflecting  
 245 the uncertainty of the predicted state estimate without  
 246 the current observation data. In contrast,  $P_{n|n}$  is the  
 247 updated covariance matrix at time  $n$ , incorporating the  
 248 current observation data, providing the most precise un-  
 249 certainty of the state estimate.  $Q$  is the process noise  
 250 covariance matrix, indicating the uncertainty of process  
 251 noise in the model. A larger  $Q$  implies greater uncer-  
 252 tainty in the system model, causing the filter to rely  
 253 more on new observation data, leading to faster response  
 254 to signal changes.  $R$  is the observation noise covariance  
 255 matrix, describing the noise level in the observation data.  
 256 A larger  $R$  makes the filter more sensitive to noise, re-  
 257 sulting in smaller gains and fewer adjustments based on  
 258 noisy observations.

259 The test signal is subjected to autoregressive suppres-  
 260 sion using the three adaptive filters described above:

262 As shown in Fig. 3, the LMS method reaches optimal  
 263 suppression more slowly compared to RLS and Kalman  
 264 filters. However, regardless of how the parameters of  
 265 RLS and Kalman filters are adjusted, the final suppres-  
 266 sion effectiveness is nearly identical across all three meth-  
 267 ods. This conclusion is further supported by the FIR tap  
 268 coefficients.

270 As shown in Fig. 4, the tap coefficients eventually con-  
 271 verge to the same value across all three methods. While  
 272 RLS and Kalman filters can achieve rapid convergence  
 273 in a short time, they involve matrix multiplications and  
 274 inversions, which typically consume significant resources  
 275 in FPGA implementations. Under these constraints, this  
 276 study selects the LMS algorithm as the adaptive filter's  
 277 core algorithm.

278 The above discussion focuses on using adaptive filters  
 279 to suppress uncertain noise. In contrast, a 2019 solution  
 280 proposed by Cornell University introduced an ANC ap-

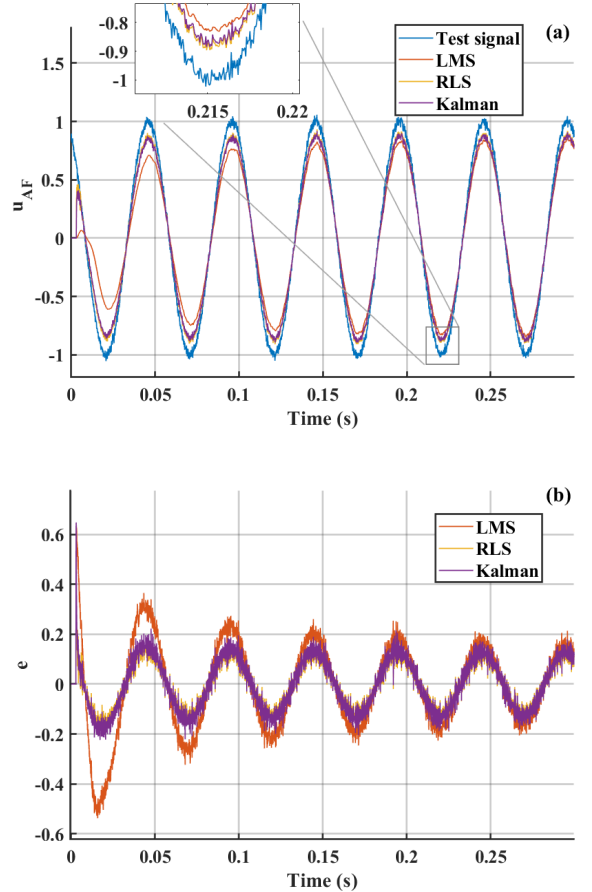


Fig. 3. (Color online) Outputs (a) and errors (b) of three adaptive filters based on the autoregressive strategy.

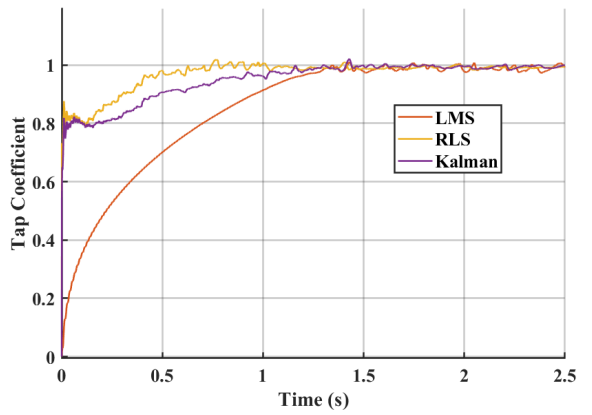


Fig. 4. (Color online) Comparison of the first tap coefficient of three adaptive filters based on the autoregressive strategy.

281 proach for RF cavities [4], which effectively suppresses  
 282 noise at fixed frequencies:

$$\left\{ \begin{array}{l} u_{\text{ANC}}(t) = \sum_m u_m(t) = \sum_m I_m(t) \cos(\omega_m t) - Q_m(t) \sin(\omega_m t) \\ I_m(n+1) = I_m(n) - \gamma \cdot \delta f_{\text{comp}}(n) \cdot \cos(\omega_m t - \phi_m(n)) \\ Q_m(n+1) = Q_m(n) + \gamma \cdot \delta f_{\text{comp}}(n) \cdot \sin(\omega_m t - \phi_m(n)) \\ \phi_m(n+1) = \phi_m(n) - \eta \cdot \delta f_{\text{comp}}(n) \cdot [I_m(n) \sin(\omega_m t - \phi_m(n)) \\ \quad + Q_m(n) \cos(\omega_m t - \phi_m(n))] \end{array} \right. \quad (7)$$

283

The output of the ANC controller, denoted as  $u_{\text{ANC}}$ , is the input to the tuner.  $u_m$  represents the ANC suppression at the  $m$ -th frequency point, which can be specifically decomposed into in-phase and quadrature components.  $\gamma$  and  $\eta$  are the learning rates of  $I_m/Q_m$  and  $\phi_m$ , respectively.  $\delta f_{\text{comp}}$  represents the frequency detuning of the cavity caused by the combined effects of Lorentz force, microphonics, and the tuner's frequency control. Here, the adaptation of  $\phi_m$  is designed to compensate for the phase of the actuator at the corresponding frequency point. It is worth noting that when  $\phi_m$  is nonzero, the closed-loop transfer function formed by ANC may exhibit loop gain greater than 1 nearby the set frequency. This results in the unintended amplification of noise at the surrounding frequencies, even though ANC significantly suppresses noise at the set frequency.

300

### C. Potential Instabilities

Adaptive filters employing autoregressive strategies must pay particular attention to potential instability issues. These primarily arise due to the absence of an external reference signal, as filter coefficient adjustments rely on historical estimation data derived from the autoregressive process. This makes the performance heavily dependent on the dynamic changes in noise and the rate of filter tap coefficients update. Specifically, if the loop delay is too large, the autoregressive non-standard reference signal may exhibit weak correlation with the current external noise signal, leading to degraded filtering performance. Additionally, the rate of change of the filter tap coefficients must be carefully considered. If the rate is too small, the filter may struggle to accurately track and suppress noise. Conversely, if the rate is too large, it can result in self-excitation and instability.

Specific parameters that need to be configured include the order of the FIR filter  $N$ , the LMS update frequency  $f_{\text{AF}}$ , and the LMS learning rate  $\mu$ . Using the cavity detuning data shown in Fig. 1 as the test noise, the following analysis focuses solely on the LMS single-loop configuration:

As shown in Fig. 5, when the filter order increases and the LMS update frequency decreases, the suppression of the main lobes in the filter remains relatively consistent. For example, at the frequency points of 50Hz and 100Hz, the closed-loop gain is almost identical. However, in the side lobe region, the gain is more refined, meaning the filter's resolution within the specified frequency range is improved, which in turn enhances noise suppression performance.

The NLMS (Normalized LMS) algorithm is proposed to address the issue of uneven coefficient update rates

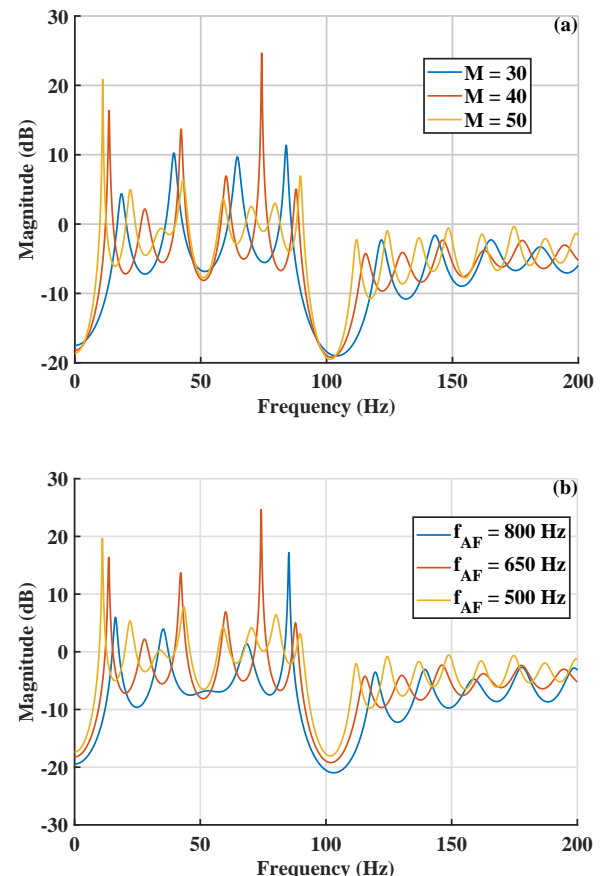


Fig. 5. (Color online) Closed-loop amplitude-frequency response curves under different filter orders (a) and LMS update frequencies (b).

caused by the LMS algorithm. The update equation for NLMS is as follows:

$$w_{n+1} = w_n + \frac{\mu}{\|x_n\|^2 + C} e(n)x_n. \quad (8)$$

In Eq. 8, the denominator of the update rate is the energy of the reference signal combined with a very small constant  $C$  (to ensure the denominator is not zero). This allows for dynamically adjusting the learning rate based on the energy of the autoregressive signal, increasing the convergence speed when the signal energy is low and decreasing it when the energy is high.

Similarly, the cavity detuning data mentioned in Fig. 1 is used as the test noise for simulation testing:

As shown in Fig. 6, compared to NLMS, LMS is more prone to instability and causing the tap coefficients to diverge, resulting in a narrower range of variability for its learning rate  $\mu$ . For example, when  $\mu = 1 \times 10^{-2}$  and  $\mu = 1 \times 10^{-3}$ , the tap coefficients diverge at 16.5s and 1s, respectively, leading to system instability. In contrast, NLMS exhibits nearly linear convergence progress before reaching stability.

It should be noted that the NLMS algorithm requires

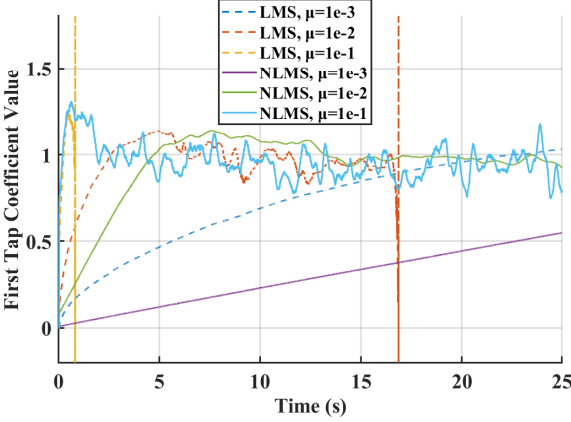


Fig. 6. (Color online) Comparison of the first tap coefficient of three adaptive filters based on the autoregressive strategy.

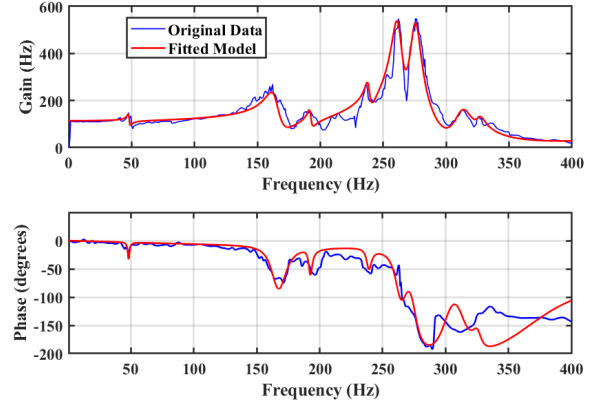


Fig. 7. (Color online) Cavity frequency detuning response to sine wave excitations of different frequencies on piezo.

357 storing historical  $N$  reference signals, which consumes a 387 tuner medium. The final fitted transfer function results  
 358 certain amount of computational resources. To address 388 are shown in Fig. 7. The magnitude-frequency response  
 359 this issue, we recommend using the NLMS algorithm to 389 is well-fitted within 400Hz, while the phase-frequency  
 360 determine the learning rate  $\mu$  during the tuning loop 390 response is accurately fitted within 300Hz. Based on  
 361 testing phase. At this stage, concerns about potential 391 the noise influence analysis in Fig. 1(b), it can be con-  
 362 system instability caused by a large  $\mu$  value can be dis- 392 cluded that the fitting range is sufficient to meet the  
 363 regarded. Once the system reaches a steady state, the 393 requirements.  
 364 optimal learning rate  $\mu$  for the LMS algorithm can be  
 365 derived accordingly.

### 366 III. SIMULATION MODEL AND TEST RESULTS

#### 367 A. Mechanical Eigenmodes of the Cavity

368 The mechanical characteristics of the cavity determine  
 369 the extent to which external forces can couple to the  
 370 eigenmodes of structure, potentially exciting unwanted  
 371 oscillations. In piezo-based detuning control, it is crucial  
 372 to measure the transfer function between the piezo drive  
 373 signal and the cavity detuning [32]. The smoothed test  
 374 results for the SHINE cavity are shown below:

375 The response transfer function contains the following  
 376 terms in the Laplace domain [33]:

$$H(s) = \left( H_0(s) + \sum_i H_i(s) \right) \cdot H_{\text{delay}}(s) \\ = \left( \frac{K_0}{\tau s + 1} + \sum_i \frac{K_i \cdot \Omega_i^2}{s^2 + \Omega_i/Q_i s + \Omega_i^2} \right) \cdot e^{-\tau_{\text{delay}} s}, \quad (9)$$

377 In Eq. 9, to account for the influence of low-frequency  
 378 and DC modes outside the measurement range, a first-  
 379 order low-pass transfer function  $H_0(s)$  is introduced,  
 380 where  $K_0$  is its gain and  $\tau$  is its time constant. Each  
 381 mechanical response modes of cavity correspond to a  
 382 second-order system  $\sum_i H_i(s)$ , where  $K_i$ ,  $\Omega_i$ , and  $Q_i$  rep-  
 383 resent the gain, resonance frequency, and quality factor  
 384 of the  $i$ -th mode, respectively.  $H_{\text{delay}}(s)$  represents the  
 385 phase shift caused by the group delay of the signal in the  
 386

387 tuner medium. The final fitted transfer function results  
 388 are shown in Fig. 7. The magnitude-frequency response  
 389 is well-fitted within 400Hz, while the phase-frequency  
 390 response is accurately fitted within 300Hz. Based on  
 391 the noise influence analysis in Fig. 1(b), it can be con-  
 392 cluded that the fitting range is sufficient to meet the  
 393 requirements.

394 What is observed in the control loop is the process that  
 395 starts with the piezo drive signal, followed by the force  
 396 applied to the tuner, resulting in cavity deformation, and  
 397 ultimately causing a change in the cavity's resonant fre-  
 398 quency. The cavity stiffness  $k_S = 3 \times 10^6 N/m$ , and the  
 399 process is illustrated in Fig. 8.

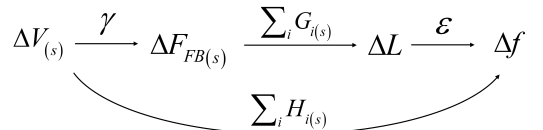


Fig. 8. Process analysis from piezo drive signal to cavity frequency detuning.

400 In mechanical dynamics, cavity deformation can be de-  
 401 composed into a set of mechanical modes. When a spe-  
 402 cific mode is excited, it produces the corresponding mode  
 403 displacement. Since the applied forces remain within the  
 404 cavity's linear elastic limit, these modes can be repre-  
 405 sented as a set of damped harmonic oscillators:

$$G_i(s) = \frac{k_i \cdot \Omega_i^2}{s^2 + \frac{\Omega_i}{Q_i} s + \Omega_i^2}. \quad (10)$$

406 Considering that the piezo response is relatively flat  
 407 below 1kHz, meaning that the force applied under the  
 408 same voltage is nearly constant across different frequen-  
 409 cies, and assuming that cavity deformation is linearly re-  
 410 lated to cavity frequency detuning ( $\varepsilon \approx 3.4 \times 10^8 Hz/m$ ),  
 411 from the Eq. 11:

$$\sum_{i=1}^n H(s)|_{s=0} = \gamma \cdot \sum_{i=1}^n G(s)|_{s=0} \cdot \varepsilon \rightarrow \sum_i K_i = \gamma \cdot \varepsilon / k_S, \quad (11)$$

we can derive the gain  $\gamma$ , and further obtain the transfer function  $G$  with the modal gains  $k_i$ .

By using the least-squares method, it is possible to approximate the forces exerted on the cavity due to microphonics, as shown in Fig. 9, which are the time-domain and frequency-domain plots of the forces.

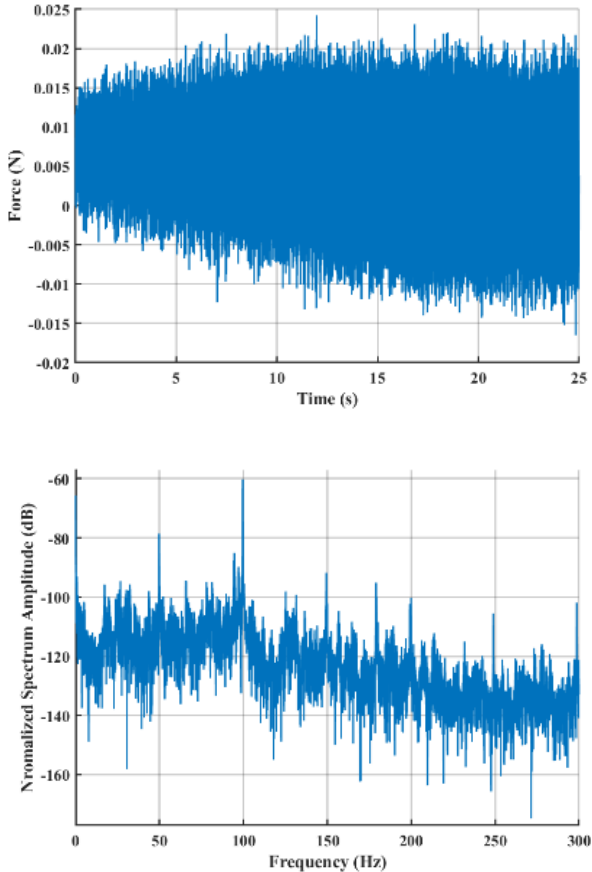


Fig. 9. (Color online) Time-domain (a) and spectrum diagrams (b) of force applied by microphonics on the cavity.

In CW mode, although the effect of LFD on the cavity frequency shift is negligible, we still incorporate it into the overall cavity mechanical model. The force exerted by the LFD on the cavity can be expressed by Eq 12.

$$F_{int} = \sum_i F_{int,i} = \sum_i \frac{k_{lfd}^i V_C^2}{k_i \varepsilon L^2}, \quad (12)$$

Here,  $k_{lfd}^i$  is the LFD constant [34], with units of  $Hz/(MVm^{-1})^2$ .

## B. Amplitude-Phase Loop and Tuning Loop in Closed-Loop Operation

During the steady-state operation of the RF system, the LLRF operates in GDR mode. In this study, various operating states of the tuning loop were observed through simulation, including open-loop, closed-loop using only the LMS algorithm, closed-loop using only the ANC algorithm, and closed-loop with both LMS and ANC loops in parallel. The impact of different tuning loop configurations on cavity detuning compensation caused by factors such as microphonics was analyzed.

First, observe the fitting performance of the tuning loop with the LMS algorithm activated, which can also be understood as the tracking capability of cavity detuning.

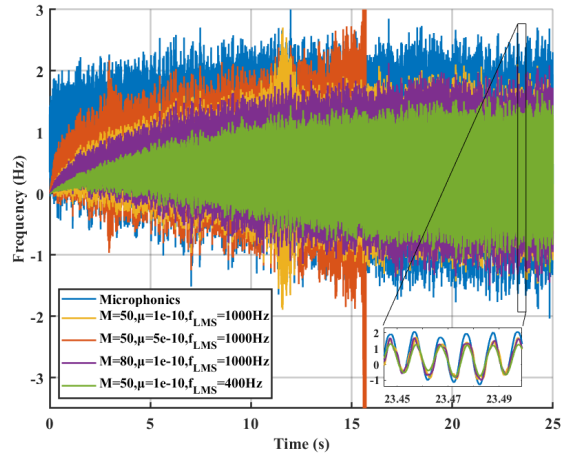
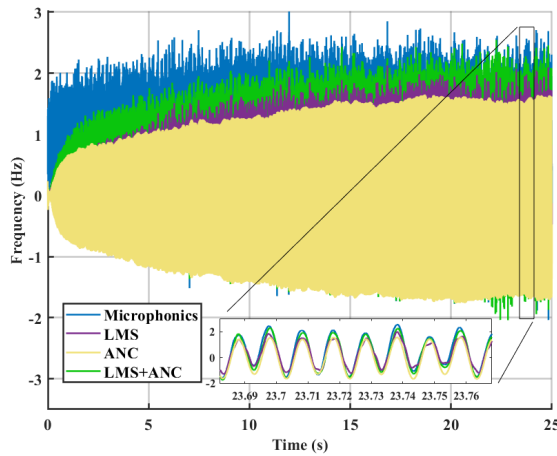


Fig. 10. (Color online) Fitting performance of tuning loops on cavity detuning for different LMS parameter combinations in closed-loop RF system.

The fitting speed of the cavity detuning by the tuning loop under different parameter configurations can be clearly observed from Fig. 10. First, using the parameter set  $M = 50$ ,  $\mu = 1 \times 10^{-10}$ , and  $f_{AF} = 1000Hz$  as the baseline (indicated by the yellow curve), the system almost becomes unstable at around 12 seconds. Then, when the learning rate  $\mu$  is increased to  $5 \times 10^{-10}$  (indicated by the red curve), although the fitting speed accelerates, the excessively large learning rate causes the cavity frequency to detune at 16 seconds, leading to divergence and eventually system instability. When the filter order is increased to 80 (indicated by the purple curve), it is evident that the system's fitting performance improves, and no abrupt changes appear during the fitting process. This suggests that increasing the filter order within a certain range helps improve the system's stability. Furthermore, when the LMS update frequency  $f_{AF}$  is adjusted to 400Hz (indicated by the green curve), although the fitting speed slows down, the final fitting performance is comparable to the baseline

466 condition. This further confirms that the optimization 504 on the cavity voltage amplitude and phase stability.  
 467 conclusions regarding the learning rate, filter order, and  
 468 LMS update frequency in the closed-loop control system  
 469 are consistent with those derived from the analysis of the  
 470 single-loop case in Sec. II C. By appropriately adjusting  
 471 the LMS parameters, the system's stability and fitting  
 472 performance can be effectively improved, and these ad-  
 473 justments are of significant guiding importance in closed-  
 474 loop systems.

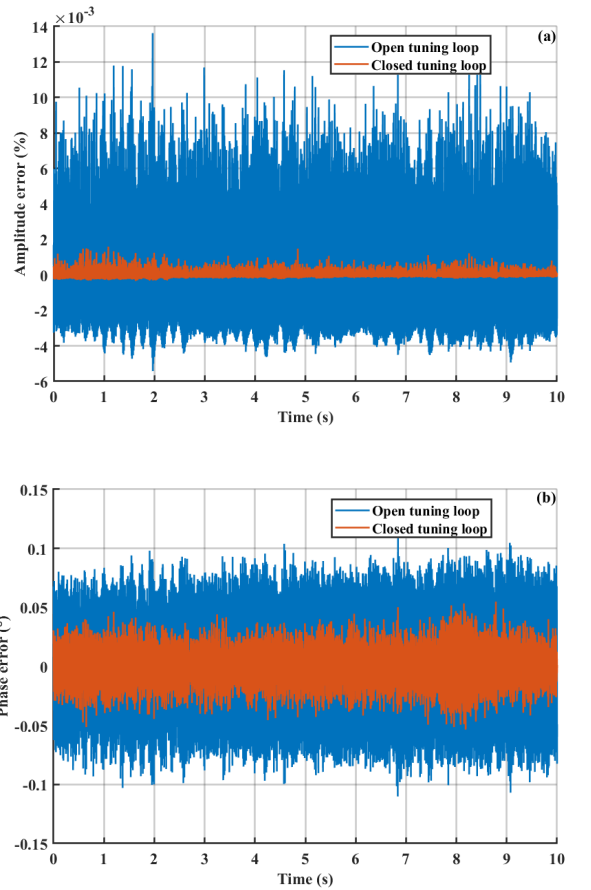
475 Incorporates the ANC algorithm to compare the fit-  
 476 ting performance of the tuning loop on cavity detuning  
 477 under three conditions: LMS only, ANC only, and the  
 478 combined effect of ANC+LMS. The ANC is designed to  
 479 suppress frequencies at 50Hz and 100Hz, while the LMS  
 480 parameter set is chosen as  $M = 80$ ,  $\mu = 1e - 10$ , and  
 481  $f_{AF} = 1000Hz$ .



482 Fig. 11. (Color online) Fitting performance of tuning loops  
 483 on cavity detuning under single LMS loop, single ANC loop,  
 484 and parallel LMS+ANC in the closed-loop RF system.

485 As shown in Fig. 11, compared to the LMS algorithm,  
 486 ANC exhibits significantly faster noise suppression at  
 487 specific frequency points. The LMS algorithm gradually  
 488 adjusts the closed-loop gain by modifying the learning  
 489 rate, thereby implementing noise suppression across the  
 490 entire frequency band. However, its suppression speed  
 491 for specific noise frequencies is relatively slow and re-  
 492 quires gradual increase to adapt to changes in other fre-  
 493 quency bands. In contrast, ANC directly targets and  
 494 suppresses specific frequency points quickly, addressing  
 495 the slow suppression effect of LMS at certain frequencies.  
 496 However, the main limitation of ANC when used alone  
 497 is its inability to track the DC component, as evidenced  
 498 by its loop fitting performance.

499 When LMS and ANC are combined, they complement  
 500 each other's weaknesses. The system is able to maintain  
 501 a high noise suppression speed while ensuring effective  
 502 suppression of low-frequency and DC components, thus  
 503 improving overall performance. Subsequently, this study  
 504 compares the impact of open-loop and closed-loop tuning



505 Fig. 12. (Color online) Amplitude (a) and phase (b)  
 506 error curves of the cavity voltage under open-loop tuning and  
 507 closed-loop tuning (LMS+ANC).

508 As shown in Fig. 12, the figure presents the ampli-  
 509 tude error (a) and phase error (b) curves under steady-  
 510 state conditions for both open-loop and closed-loop tun-  
 511 ing (with LMS+ANC), with data recorded over a 10-  
 512 second interval. The RMS values of amplitude error for  
 513 the two configurations are 0.0033% and 0.0002%, respec-  
 514 tively, while the RMS values of phase error are 0.0498°  
 515 and 0.0138°, respectively.

516 From the data, it is evident that even under the open-  
 517 loop tuning condition, the amplitude error can reach the  
 518 target only through the amplitude-phase loop; however,  
 519 the phase stability requirements are far from being met.

520 In contrast, under closed-loop tuning (LMS+ANC),  
 521 both the amplitude and phase errors are significantly re-  
 522 duced, indicating that the closed-loop tuning system can  
 523 better enhance the system's stability and meet stringent  
 524 accuracy requirements. This confirms the important role  
 525 of combining LMS and ANC in noise suppression and  
 526 system optimization.



639 cal design, fabrication and tests of dressed 650 MHz 2- 667 [28] R.T. Keshwani, S. Mukhopadhyay, R.D. Gudi et al.,  
 640 cell superconducting cavities for CEPC. Nucl. Instrum. 668 Comparative investigations on detuning estimator for  
 641 Methods Phys. Res., Sect. A 1031, 166590 (2022). doi: 669 experimental RF cavity. IEEE Trans. Instrum. Meas. 72  
 642 [10.1016/j.nima.2022.166590](https://doi.org/10.1016/j.nima.2022.166590) 670 (2023). doi: [10.1109/TIM.2023.3311075](https://doi.org/10.1109/TIM.2023.3311075)

643 [22] X. Li, H. Sun, C.L. Zhang et al., Design of rapid tuning 671 [29] Z. Gao, Y. He, W. Chang et al., A new microphonics  
 644 system for a ferrite-loaded cavity. Radiat. Detect. Tech- 672 measurement method for superconducting RF cavities.  
 645 nol. Methods 5, 324-331 (2021). doi: [10.1007/s41605-021-00274-7](https://doi.org/10.1007/s41605-021-00274-7) 673 Nucl. Instrum. Methods Phys. Res., Sect. A 767, 212-  
 646 674 217 (2014). doi: [10.1016/j.nima.2014.08.030](https://doi.org/10.1016/j.nima.2014.08.030)

647 [23] P.P. Gong, Y.B. Zhao, H.T. Hou et al., Tuning control 675 [30] S.N. Simrock, Lorentz force compensation of pulsed SRF  
 648 system of a third harmonic superconducting cavity in 676 cavities. Proc. Int. LINAC Conf. 2002 (2002).

649 the Shanghai Synchrotron Radiation Facility. Nucl. Sci. 677 [31] C.T. Somefun, S.A. Daramola, T.E. Somefun, Advance-  
 650 Tech. 30, 157 (2019). doi: [10.1007/s41365-019-0655-4](https://doi.org/10.1007/s41365-019-0655-4) 678 ments and applications of adaptive filters in signal pro-  
 651 [24] Y. Zong, J.F. Chen, D. Wang et al., Accelerating 679 cessing. J. Eng. Sci. Appl. 2024, 1259-1272 (2024). doi:  
 652 gradient improvement in nitrogen-doped superconduct- 680 [10.1016/j.nima.2023.168724](https://doi.org/10.1016/j.nima.2023.168724) 681

653 [25] J.R. Delahaye, Phase and amplitude stabilization of 681 [32] X.F. Huang, Y. Sun, G.W. Wang et al., Measurement  
 654 beam-loaded superconducting resonators. Proc. Int. 682 of the transfer function for a spoke cavity of C-ADS  
 655 LINAC Conf. 1992, 16 (1992). 683 Injector I. Chin. Phys. C 41(4), 047001 (2017). doi:  
 656 [26] Z.K. Liu, C. Wang, L.H. Chang et al., Modeling 684 [10.1088/1674-1137/41/4/047001](https://doi.org/10.1088/1674-1137/41/4/047001)

657 the interaction of a heavily beam loaded SRF cavity 685 [33] A. Neumann, W. Anders, O. Kugeler et al., Analysis  
 658 with its low-level RF feedback loops. Nucl. Instrum. 686 and active compensation of microphonics in continuous  
 659 Methods Phys. Res., Sect. A 894, 57-71 (2018). doi: 687 wave narrowband superconducting cavities. Phys. Rev.  
 660 [10.1016/j.nima.2018.03.046](https://doi.org/10.1016/j.nima.2018.03.046) 688 ST Accel. Beams 13, 082001 (2010).

661 [27] T. Schilcher, Vector sum control of pulsed accelerating 689 [34] A. Bellandi, J. Branlard, A. Eichler et al., Integral reso-  
 662 fields in Lorentz force detuned superconducting cavities. 690 nance control in continuous wave superconducting par-  
 663 PhD Thesis (1998). 691 ticle accelerators. IFAC-PapersOnLine 53(2), 361-367  
 664 692 (2020). doi: [10.1016/j.ifacol.2020.12.186](https://doi.org/10.1016/j.ifacol.2020.12.186)